



Triple perovskite structured $\text{Nd}_{1.5}\text{Ba}_{1.5}\text{CoFeMnO}_{9-\delta}$ oxygen electrode materials for highly efficient and stable reversible protonic ceramic cells

John-In Lee^a, Ka-Young Park^a, Hyunyoung Park^{a,d}, Hohann Bae^b, Muhammad Saqib^a, Kwangho Park^a, Ji-Seop Shin^a, Minkyong Jo^a, Jongsoon Kim^{a,d}, Sun-Ju Song^{b,*}, Eric D. Wachsman^{c,**}, Jun-Young Park^{a,***}

^a HMC, Department of Nanotechnology and Advanced Materials Engineering, Sejong University, Seoul, 05006, South Korea

^b Department of Materials Science and Engineering, Chonnam National University, Gwangju, 61186, South Korea

^c Maryland Energy Innovation Institute, Department of Materials Science and Engineering, University of Maryland, College Park, MD, 20742, United States

^d Department of Energy Science, Sungkyunkwan University, Suwon 03063, South Korea

HIGHLIGHTS

- Highly hydrated triple-conducting electrode with triple perovskite structure.
- High oxygen defective NBCFM with the rapid reaction rates for oxygen electrodes.
- Outstanding performance of NBCFM for steam and air electrodes of RPCCs.
- Mechanistic study of the superior performance of NBCFM oxygen electrode.

ARTICLE INFO

Keywords:

Reversible protonic ceramic cells
Triple perovskite
Hydration
Triple-conducting oxide
Oxygen electrode

ABSTRACT

The sluggish kinetics of oxygen electrode reactions represent one of the most significant barriers to realizing effective reversible protonic ceramic cells (RPCCs) at intermediate temperatures. Maximization of oxygen ion and proton conduction characteristics through hydration of electron-conducting solid oxides is a key technology that can solve this issue. We report on the exceptional performance at the oxygen electrode in RPCCs achieved using a highly defective material with excessive oxygen nonstoichiometry, $\text{Nd}_{1.5}\text{Ba}_{1.5}\text{CoFeMnO}_{9-\delta}$ (NBCFM). Use of this material enables a superior reaction rate and conductivity during oxygen electrode reactions, maximizing the concentration of protons (with a high degree of hydration) as a guest ion as well as intrinsic oxygen vacancies. The peak power densities of this NBCFM cell are quite high, and a 1.4 V electrolyzing potential is achieved by NBCFM at $-2.34 \text{ A}\cdot\text{cm}^{-2}$ at 600 °C. Furthermore, these NBCFM cells are stable under prolonged (960 h) continuous operation at 600 °C.

1. Introduction

As fossil fuels are replaced with inherently intermittent renewable energy sources, there is an increased need for effective storage and delivery methods that can provide electricity from these renewable sources on demand [1,2]. In this context, reversible electrochemical cell technology is receiving a great deal of attention due to its great potential to fulfill this role. The promise of electrochemical cells stems from their

offer of high conversion efficiency, low environmental impact, and flexibility between power-to-gas (P2G) and gas-to-power (G2P) systems [3–8]. In particular, reversible solid oxide cells based on proton-conducting electrolytes at intermediate temperatures (IT < 700 °C) are a novel, cost-effective possibility for reversible interchange of chemical to electrical energy with high efficiency [9]. Theoretically, reversible protonic ceramic cells (RPCCs) have the ability to produce pure H_2 directly at reduced temperatures. This ability comes from the

* Corresponding author.

** Corresponding author.

*** Corresponding author.

E-mail addresses: song@chonnam.ac.kr (S.-J. Song), ewach@umd.edu (E.D. Wachsman), jyoung@sejong.ac.kr (J.-Y. Park).

higher ionic conductivity of proton-conducting electrolytes and low activation energy in comparison to oxygen ion-conducting electrolytes at these reduced temperatures [10].

O'Hayre et al. [11] demonstrated the exceptional performance and durability of protonic ceramic fuel cells (PCFCs) by testing a total of 11 different fuels at 500–600 °C. They also proposed a triple conducting ($H^+/O^{2-}/e^-$) PCFC-compatible $BaCo_{0.4}Zr_{0.1}Fe_{0.4}Y_{0.1}O_{3-\delta}$ (BCZFY) perovskite cathode with a $BaCe_{0.7}Zr_{0.1}Y_{0.1}O_{3-\delta}$ (BCZYYb) electrolyte, with which they achieved a power density as high as 0.455 $W\cdot cm^{-2}$ at 500 °C [12]. For hydrogen production under protonic ceramic electrolysis cell (PCEC) mode, Kim et al. [13] achieved $-1.19 W\cdot cm^{-2}$ at 1.4 V and 600 °C by employing a BCZYYb electrolyte with the $NdBa_{0.5}Sr_{0.5}Co_{1.5}Fe_{0.5}O_{5+\delta}$ (NBSCF) cathode material. The Haile group [14] also reported a remarkable current density of $-3.23 A\cdot cm^{-2}$ at 1.4 V and 600 °C in microstructurally optimized cells (via pulsed laser deposition), based on a high-activity $PrBa_{0.5}Sr_{0.5}Co_{2-x}Fe_xO_{5+\delta}$ (PBSCF) electrode. However, despite these recent advancements in materials and ceramic processing, a large discrepancy still exists between the

theoretical and attained performances of RPCCs, particularly PCEC performance. One of the main sources of this performance discrepancy is that the kinetics of oxygen electrode reactions, the oxygen evolution reaction (OER) and oxygen reduction reaction (ORR), are intrinsically sluggish at reduced temperatures [15,16].

Hence, intensive research is needed in an effort to identify novel bifunctional materials that are suitable for RPCC operation. Among the various oxides offering high mixed ionic and electronic conductivities (MIEC), perovskites are the subject of renewed interest due to their potential as bifunctional oxygen electrode materials [17]. These include BCZFY [12], NBSCF [13], and $BaGd_{0.8}La_{0.2}Co_2O_{6-\delta}$ (BGLC) [18]. Maximization of oxygen ion and proton conduction characteristics through hydration of electron-conducting perovskite oxides is a key strategy that can solve the sluggish kinetics of oxygen electrode reactions for RPCCs at IT, which require oxygen ion- and proton-coupled electron transfer (*i.e.* triple conduction of $H^+/O^{2-}/e^-$) [11,13]. Previous studies reported that some base cation-containing oxides (*e.g.* $BaCeO_3$ and $SrZrO_3$) can introduce protons through a pure acid-base reaction [9], but in most

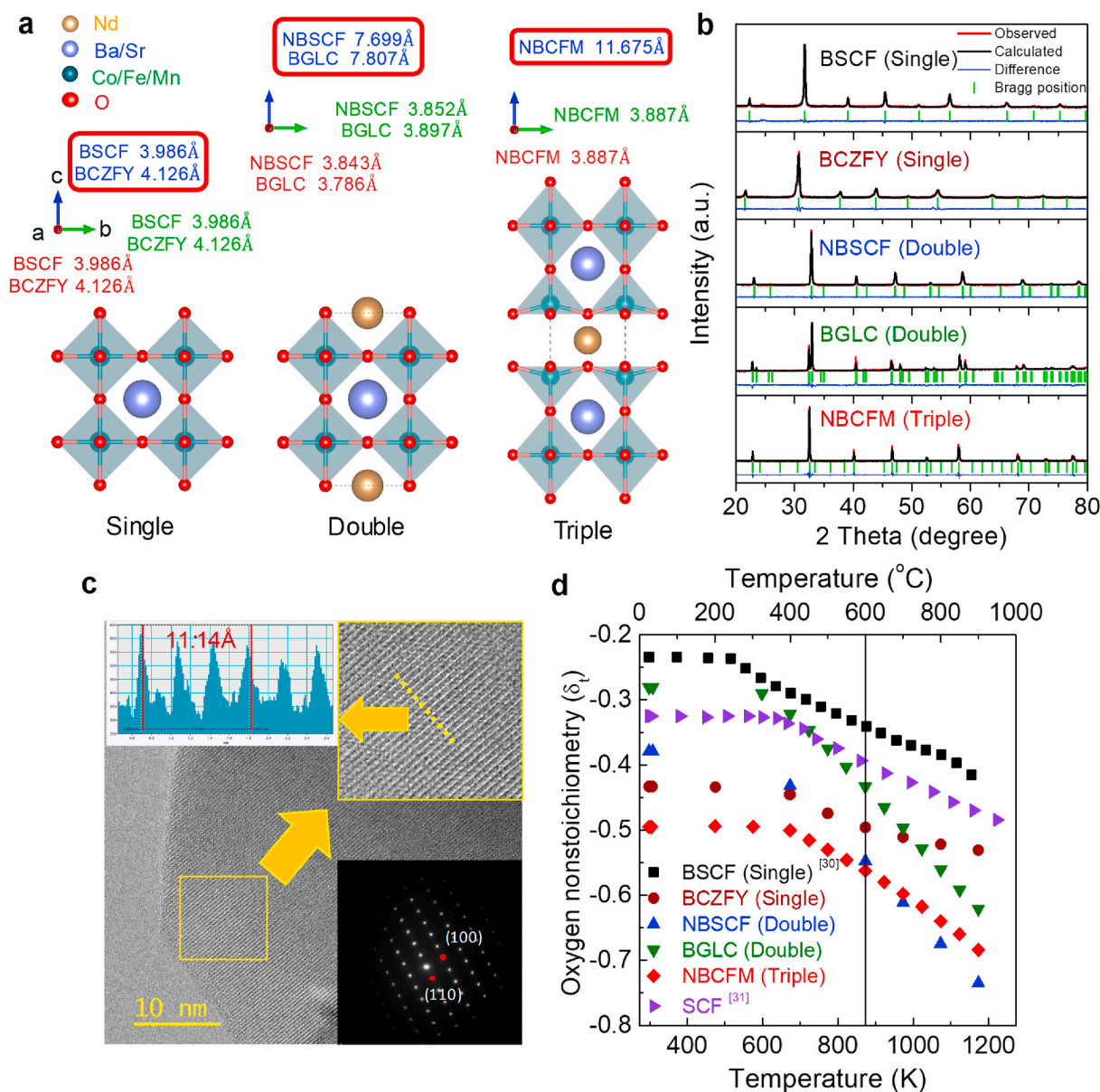


Fig. 1. Structural characteristics of the perovskite materials. (a) Representative of the single, double and triple perovskite structures with lattice constants. (b) XRD patterns of BSCF, BCZFY, NBSCF, BGLC, and NBCFM with their Rietveld refinement results. a.u., arbitrary units. (c) HR-TEM image with SAED pattern of NBCFM. (d) Measured oxygen nonstoichiometry (plotted as δ_i) of perovskite materials as a function of temperature.

cases the degree of hydration is very small or limited to the oxygen vacancy concentration in anion sublattices [15]. Very recently, we introduced a novel triple perovskite, $\text{Nd}_{1.5}\text{Ba}_{1.5}\text{CoFeMnO}_{9.8}$ (NBCFM), for use as a highly active and durable bifunctional oxygen electrocatalyst in unitized reversible fuel cells and in metal-air batteries at room temperature [19]. The triple perovskite NBCFM structure was created by stacking three single perovskite blocks (cubic axes tripled along the *c*-axis) (Fig. 1a and Fig. S1a–c). This material was realized by engineering of the material's composition and electronic configuration in the perovskites. However, the core elements of ion engineering for high-temperature electrochemical ceramic cells were not identified in this paper. In particular, there has been little research on materials that can maximize oxygen ion and proton conduction through hydration of electron-conducting solid oxides at high temperatures.

Herein, as a highly defective material with excessive oxygen nonstoichiometry, NBCFM is exploited for the first time as a bifunctional air (steam) electrode material for RPCCs at elevated temperatures (500–700 °C). NBCFM achieved a very high degree of hydration, maximizing the concentration of protons as a guest ion as well as intrinsic oxygen vacancies. NBCFM shows an outstanding area specific resistance (ASR) value of 0.98 $\Omega\cdot\text{cm}^2$ at 600 °C (IT). The peak power densities (PPDs) of the NBCFM cells are very high, 0.16–1.37 $\text{W}\cdot\text{cm}^{-2}$ at 500–700 °C in PCFCs, which are approximately 2–3 times greater than the PPD of $\text{Ba}_{0.5}\text{Sr}_{0.5}\text{Co}_{0.8}\text{Fe}_{0.2}\text{O}_{3.8}$ (BSCF) and BGLC cells. In PCEC mode, the current densities of cells with the NBCFM steam electrode at different applied voltages are much higher than those of cells with other electrodes at each operating temperature tested. A number of important parameters that affect OER and ORR performance have been identified and can now be considered in the design of future high-performance NBCFM-based RPCCs [19–23].

2. Experimental section

2.1. Synthesis of cell components

For the air (steam) electrode materials, BSCF, BCZFY, NBSCF, BGLC, and NBCFM powders were synthesized using a solid-state method from Nd_2O_3 (99.9% purity, Alfa Aesar), BaCO_3 (99% purity, Alfa Aesar), SrCO_3 (99.9% purity, Sigma-Aldrich), Co_3O_4 (99.7% purity, Alfa Aesar), Fe_2O_3 (99.85% purity, Alfa Aesar), ZrO_2 (99.5% purity, Alfa Aesar), Y_2O_3 (99.9% purity, Alfa Aesar), Gd_2O_3 (99.9% purity, Alfa Aesar), La_2O_3 (99.99% purity, Yakuri pure chemicals, Japan) and MnO_2 (99.9% purity, Alfa Aesar). Stoichiometric amounts of the starting materials were ball-milled in ethanol using zirconia balls for 24 h. All the perovskite materials were calcined at 970–1250 °C for 3–10 h. NDC powders for the composite air (steam) electrodes were prepared using the glycine-nitrate combustion method from $\text{Ce}(\text{NO}_3)_3\cdot 6\text{H}_2\text{O}$ (99.99% purity, Alfa Aesar) and $\text{Nd}(\text{NO}_3)_3\cdot 6\text{H}_2\text{O}$ (99.99% purity, Alfa Aesar). These nitrate hexahydrates, in the required molar ratio, were dissolved in deionized water with glycine (99.5% purity, Alfa Aesar), heated on a hot plate until they changed to yellow ash and caught in flames, and then fired at 700 °C for 2 h. For the anode and electrolyte materials, NiO and BCZYYb powders were procured from Kceracell (Korea).

2.2. Characterization of cell components

To investigate the phase identification and crystal structure of the cell components, the as-prepared powders were analyzed using a powder X-ray diffractometer (XRD, X'Pert, PAN analytical) with the Rietveld refinement method (FullProf software). High-temperature XRD analysis was also carried out to ascertain the structural robustness of the NBCFM

under RPCC operating conditions from room temperature to 800 °C at 5 °C $\cdot\text{min}^{-1}$. The microstructures of the cell components were investigated by field emission-scanning electron microscopy (FESEM, Hitachi, SU8010, 15 KV) and high-resolution transmission electron microscopy (HRTEM, JEOL, JEM-2100F, 200 KV). The chemical compositions of the component phases were analyzed using an EDX system equipped to the HRTEM equipment. Average linear thermal expansion coefficients (TECs) were measured by using a dilatometer (LINSEIS, L75) in the temperature range from room temperature to 1,000 °C with a heating/cooling rate of 5 °C $\cdot\text{min}^{-1}$ in air.

2.3. Determination of oxygen nonstoichiometry

The electronic structure and chemical identification of all the perovskite materials were determined by X-ray photoelectron spectrometer (XPS, K-Alpha+, Thermo Scientific) analysis using an Al K α x-ray source, micro-focused monochromator. The oxygen ($\text{O}_2^-/\text{O}^\ominus$) and cobalt ($\text{Co}^{4+}/\text{Co}^{3+}$) species in the perovskite materials were analyzed to find the relative concentrations of surface oxygen defects in the perovskite materials. The oxygen nonstoichiometry (δ_p) of the perovskite materials was determined by a high precision thermogravimetric analysis (TGA) set-up equipped with a Cahn D200 microbalance, all values were measured as a function of temperature at a constant flow rate of 200 sccm in air. For measurements in wet conditions, the specimen was first annealed under dry gas for 24 h, passed through a coiled cold trap zone to remove any water vapor present in the gas. The water vapor pressure was measured by dew-point meter (DM70, Vaisala Oyj, Finland). The square-bar type ($6 \times 6 \times 4 \text{ mm}^3$) specimen was prepared by uniaxial pressing followed by heat treatment at 900 °C for 2 h in air. According to the TGA results and initial oxygen nonstoichiometry (δ_o), which was evaluated using the iodometric titration method, the relationship between the oxygen nonstoichiometric variation (δ_i) and measured weight change (Δw) was calculated by;

$$\delta_i = \delta_o + \frac{\Delta w(M_s - M_o\delta_o)}{M_o w_s} \quad (1)$$

where w_s is the initial specimen weight, M_o is the oxygen atomic weight, and M_s is the molecular formula weight (molar weight) of the specimen. For the δ_o of the perovskite materials at room temperature, 20 mg of powder was dissolved in 3.5 N HCl with potassium iodide (KI, Alfa Aesar) and starch was used as an indicator. Then, the solution was titrated with 0.025 N sodium thiosulfate ($\text{Na}_2\text{S}_2\text{O}_3$, Daejung) until the solution color began to change.

2.4. Measurements of electrical conductivity

A DC 4-probe method was used to measure the electrical conductivity of the perovskite-based specimens in air (200 sccm). The samples were prepared by pressing the powders followed by sintering at 1200–1300 °C for 4–10 h to fabricate dense bars (>95% of the theoretical density). The electrical conductivity was measured using a potentiostat/galvanostat (VSP, Bio-Logic). Moreover, chemical diffusion coefficients of the perovskite materials were determined by electrical conductivity relaxation (ECR) experiments on thin rectangular slabs as a function of oxygen partial pressure ($-2.0 \leq \log(P_{\text{O}_2}/\text{atm}) \leq -0.68$) and water partial pressure ($-1.522 \leq \log(P_{\text{H}_2\text{O}}/\text{atm}) \leq -0.523$) using O_2 and N_2 gas mixtures at 500–750 °C. When the P_{O_2} and $P_{\text{H}_2\text{O}}$ was abruptly changed to a new value, the specimens were allowed to completely equilibrate in the new thermodynamic conditions.

2.5. Fabrications of NiO-BCZYYb supported RPCCs

The NiO-BaCe_{0.7}Zr_{0.1}Y_{0.1}Yb_{0.1}O_{3-δ} (BCZYYb) supported reversible protonic ceramic cells were fabricated using the tape-casting method. NiO-BCZYYb (65:35 wt% ratio) powders were dispersed in ethanol with polymethyl methacrylate (PMMA, 10 wt%, Alfa Aesar), toluene (Sigma-Aldrich), fish oil (Sigma-Aldrich), polyethylene glycol (PEG8000, Fisher Scientific) and polyvinyl butyral (PVB, Sigma-Aldrich), before ball milling for 48 h. After de-gassing, the slurries were cast automatically (STC-14A, Hansung Systems) onto a Mylar sheet to fabricate a green tape with a thickness of 450 μm. After drying, the green tapes were cut into round pieces (diameter of 25 mm) and then pre-sintered at 900 °C for 2 h. Slurries of the functional layer were prepared by mixing NiO, BCZYYb, PVB, Solsperse (SG24000, Lubrizol), and Di-n-butyl phthalate (DBP, Sigma Aldrich) for 48 h, these were then coated onto the pre-sintered NiO-BCZYYb substrate and heat-treated at 400 °C for 2 h. Similarly, the BCZYYb electrolyte slurries were prepared by mixing BCZYYb powder with PVB, Solsperse and DBP, before ball milling for 48 h. The electrolyte slurries were deposited onto the pre-sintered NiO-BCZYYb functional layer side several times using the drop-coating technique and then sintered at 1450 °C for 4 h. Air electrode slurries were prepared by mixing a perovskite material with ESL 441 vehicle (ESL ElectroScience) using a mortar and pestle. The air electrode ink was screen-printed on the BCZYYb electrolyte side of the anode-supported cells and then sintered at 1100 °C for 2 h. Silver mesh and gold wires were used as the current collector and leads, respectively.

2.6. Electrochemical measurements of NiO-BCZYYb supported cells

The operation characteristics of the anode-supported cells were controlled by a fuel cell test station (NARA Cell Tech Co.) equipped with an electrical load (PLZ-164WA, KiKusui Electronics Co.), mass flow controllers, and an alumina reactor. A ceramic adhesive (Ceramabond 668, Aremco) was used to seal the single cells. Current–voltage (I–V) polarization curves were measured in galvanostatic mode at 500–700 °C. In PCFC operation mode, humidified H₂ (3% H₂O) was applied to the anode side as a fuel through a water bubbler with a flow rate of 200 sccm, while ambient air was supplied as an oxidant to the cathode. Under the steam PCEC mode, steam diluted with ambient air (steam:air = 20:80) was introduced to the steam (air) electrode after going through a bubbler with a constant flow rate of 200 sccm. In the hydrogen electrode, 10% hydrogen in N₂ was fed into the hydrogen electrode. The electrical conductivity was determined by electrochemical impedance spectroscopy (EIS) using a potentiostat or galvanostat instrument in the frequency range from 1 MHz to 0.1 Hz. The long-term operation of the Ni-BCZYYb anode-supported cells was tested using a constant current mode of 0.2 A·cm⁻² (fuel cell mode) and -0.2 A·cm⁻² (electrolysis mode) at 600 °C.

2.7. DFT calculations

We performed first-principles calculations based on density functional theory (DFT) using the Vienna ab initio simulation package (VASP) [24]. All DFT calculations were performed with Pseudopotentials of projector augmented-wave (PAW) [25], Perdew–Burke–Ernzerhof (PBE) functional [26], and the generalized gradient approximations (GGA)+U [27]. Effective Hubbard-*U* parameters of 3.5, 3.5, 5.5, and 3.9 eV were used for the 3*d* electrons of Co, Fe, Ni, and Mn, respectively, this arrangement was determined from previous papers [28]. Various configurations among the metal ions and oxygen/vacancy orderings in BCZFY, BSCF, NBCFM, and NBSCF were generated using CASM software [29]. For the first principles calculations, we prepared various simplified structural models, such as BaCo_{0.375}Zr_{0.125}Fe_{0.375}Y_{0.125}O_{2.5} for BCZFY, Ba_{0.5}Sr_{0.5}Co_{0.75}Fe_{0.25}O₃ for BSCF, Nd_{1.5}Ba_{1.5}CoFeMnO_{8.33} for NBCFM, and NdBa_{0.5}Sr_{0.5}Co_{1.33}Fe_{0.67}O₆ for NBSCF. We determined the most stable structures among

the samples through comparison of the electrostatic energies and DFT energies. A plane-wave basis set was used with an energy cutoff of 500 eV, appropriate k-point meshes were selected to ensure that the total free energy of the system converged within 0.1 meV.

3. Results and discussion

3.1. Characterizations of perovskite structured electrode materials

Fig. 1b shows the x-ray diffraction (XRD) patterns of the perovskite-based materials as well as their Rietveld refinement results. All peaks were identified as perovskite-based structures without any secondary phases. The crystal structures (space group) of BSCF, BCZFY, NBSCF, BGLC, and NBCFM were indexed as cubic (*Pm* $\bar{3}$ *m*), cubic (*Pm* $\bar{3}$ *m*), orthorhombic (*Pmmm*), orthorhombic (*Pmmm*), and tetragonal (*P4/mmm*), respectively (Table 1). The *c*-axis lattice constants of the perovskites, calculated by the Rietveld refinements, showed remarkable differences, with a progressive increase from 3.986 (4.126) Å to 7.699 (7.807) Å, and then to 11.675 Å for single (BSCF, BCZFY), double (NBSCF, BGLC), and triple perovskites (NBCFM), respectively (Fig. S1d). The results of Rietveld refinement are shown in Table 1 and the low reliability factors ($R_{wp} = 6.42\%$, $R_p = 3.95\%$, $\chi^2 = 7.50$) for NBCFM indicate a good fit between the experimental and calculated XRD patterns. To ascertain structural robustness of the NBCFM under RPCC operating conditions, high-temperature XRD analysis was also carried out from room temperature to 800 °C at 5 °C·min⁻¹ (Fig. S1e). Results demonstrated that the NBCFM was thermodynamically stable as a triple perovskite crystal structure without any secondary phases at elevated temperatures.

The triple perovskite structure of NBCFM was also further confirmed by the selected area electron diffraction (SAED) pattern observed from the [001] zone axis of the high-resolution transmission electron microscopy (HR-TEM) image (Fig. 1c). The repeated layers along the *c*-axis were determined to be at 11.14 Å (Fig. 1c, inset) using a simulation of the relative intensity of each atomic column, this is similar to the results obtained from the Rietveld refinement results. On the other hand, the average *c*-axis lattice parameter was 3.50 and 7.65 Å for BSCF (single) and NBSCF (double), respectively, indicating that NBCFM has a three layers of single perovskite structures (Figs. S2a–b). The HR-TEM and field emission-scanning electron microscopy (FE-SEM) images of NBCFM exhibit sub-micron sized (100–600 nm) agglomerated and round particle morphology (Fig. S2c). Elemental mapping images of the NBCFM powder present that the constituent elements are uniformly distributed throughout the particles (Fig. S2d).

The extended *c*-axis that comes from the double- and tri-layer structure of single perovskite originates from the doping of lanthanide (A-site) and transition metals (B-site) in the ABO₃ perovskite system, with the formation of extra oxygen vacancies to maintain charge neutrality conditions. As shown in Fig. 1d, the oxygen nonstoichiometry, δ_t values, of BSCF, BCZFY, NBSCF, BGLC and NBCFM at 600 °C were determined to be 0.341, 0.496, 0.547, 0.433 and 0.562 [cf. SrCo_{0.8}Fe_{0.2}O_{3-δ} (SCF): 0.398] [30,31], respectively, as calculated by the iodometric titration method and high precision thermogravimetric analysis (TGA). A considerable change in the average oxidation state of B-site cations was also found for the triple perovskite, as seen in Fig. S1f. This shows that the triple perovskite NBCFM material contains plentiful oxygen vacancies under the operating conditions of RPCCs, this plays an important role in oxygen electrode activities for RPCCs.

3.2. Reversible protonic ceramic cell design

To investigate the oxygen electrode performances of the perovskite materials, NiO-BCZYYb electrode-supported cells were fabricated with the BCZYYb electrolyte. Fig. 2a shows the XRD patterns of NiO-BCZYYb, all peaks correspond to NiO and BCZYYb phases without other phases or

Table 1

Crystal structure parameters (with TECs) of the perovskite materials based on Rietveld refinements and TGA measurements.

Materials	BSCF(Single)	BCZFY(Single)	NBSCF(Double)	BGLC(Double)	NBCFM(Triple)
Space group(phase structure)	$Pm\bar{3}m$ (cubic)	$Pm\bar{3}m$ (cubic)	$Pmmm$ (orthorhombic)	$Pmmm$ (orthorhombic)	$P4/mmm$ (tetragonal)
Lattice parameter (a, Å)	3.986	4.126	3.843	3.786	3.887
Lattice parameter (b, Å)	3.986	4.126	3.852	3.897	3.887
Lattice parameter (c, Å)	3.986	4.126	7.699	7.807	11.675
Reliability factors (R_p , %)	1.52	2.67	1.81	2.49	3.95
Reliability factors (R_{wp} , %)	1.97	3.60	2.35	4.04	6.42
Reliability factors (χ^2)	1.57	2.93	1.79	3.84	7.50
Oxygen deficiency (δ_t , 600 °C)	0.341	0.496	0.547	0.433	0.562
TEC ($\times 10^6$ K ⁻¹)	17.8	18.1	24.9	21.0	13.1

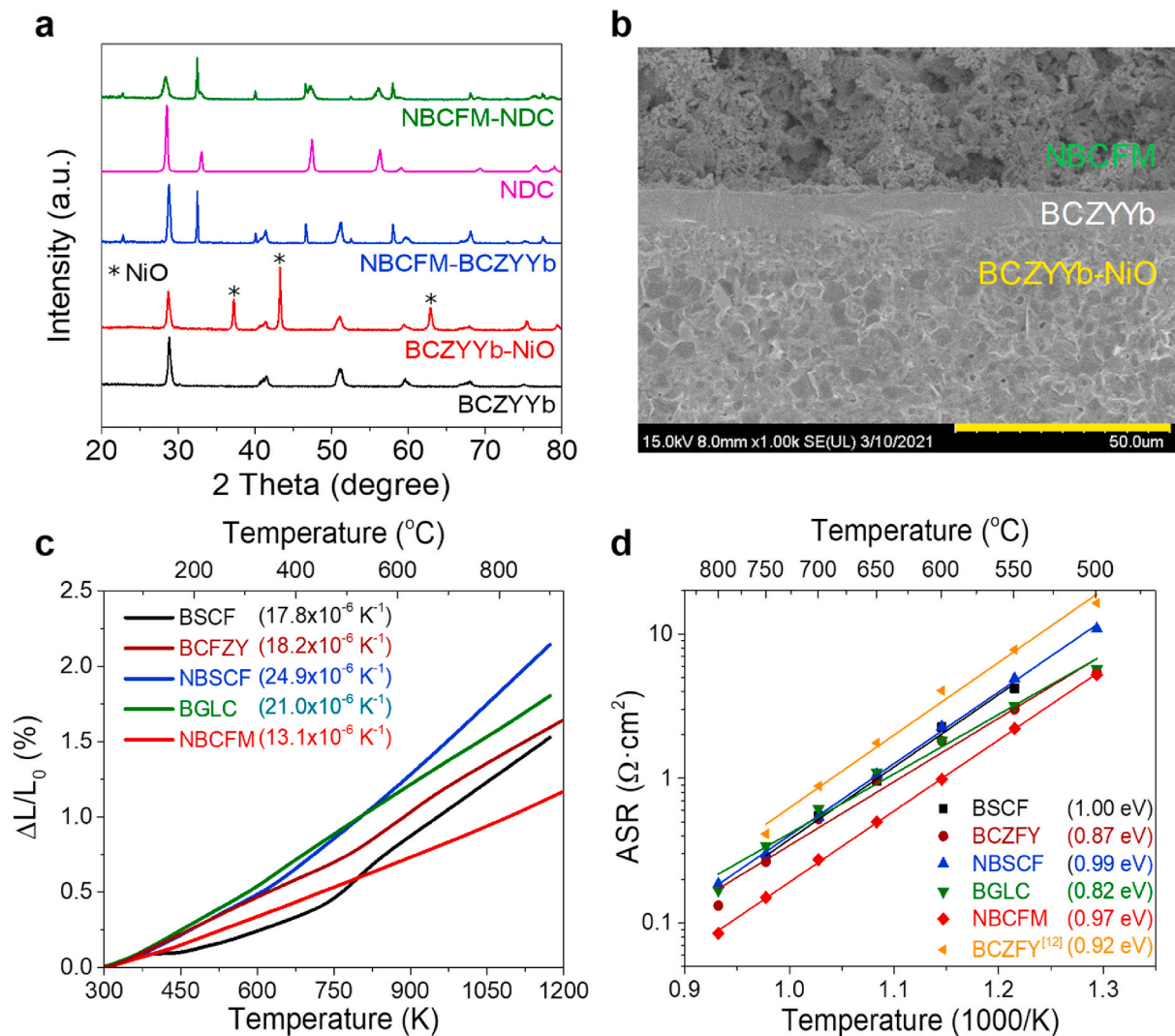


Fig. 2. Physiochemical characteristics of the cell components. (a) XRD patterns of BCZYYb (electrolyte), NiO-BCZYYb (fuel electrode), NBCFM-NDC, NDC, and NBCFM-BCZYYb powders (composite air electrode). (b) Cross-sectional microstructure of the NiO-BCZYYb supported cell (BCZYYb electrolyte) with the NBCFM air (steam) electrode examined by using FE-SEM. (c) TEC values of perovskite materials. (d) Comparison of the electrode area specific resistances (ASRs) of NBCFM symmetric cell in this work as a function of temperature with those of other perovskite materials.

impurities. The BCZYb electrolyte powders formed a single phase with the perovskite structure. The XRD patterns of the $\text{Nd}_{0.1}\text{Ce}_{0.9}\text{O}_{2-\delta}$ (NDC) powders after calcination confirm that the samples were crystallized into a fluorite structure with no unknown extra peaks. NDC was selected as the composite (NBCFM-NDC) air electrode material to expedite the reaction of triple ($\text{H}^+/\text{O}^{2-}/\text{e}^-$) conducting at the interface between the proton-conducting electrolyte and MIEC materials for PCFCs [16]. We also tested pure NBCFM and composite NBCFM-BCZYb as air electrode materials for RPCCs.

The cross-sectional microstructure of the NiO-BCZYb cell with the BCZYb electrolyte and composite perovskite air electrode was examined using FE-SEM and the results are shown in Figs. 2b and S3. It can be clearly observed that the NiO-BCZYb is composed of a supporting layer and functional layer with macro- and micro-pores due to the addition of the pore former. The electrolyte layer was entirely dense without any pinholes, while the composite perovskite cathode layer with a sufficiently porous structure is continuously attached to the electrolyte layer. The thermal compatibility between components is an important parameter when fabricating RPCCs in terms of reducing fabrication costs and improving durability [32,33]. As shown in Fig. 2c, the thermal expansion coefficient value of NBCFM is $13.1 \times 10^{-6} \text{ K}^{-1}$, this is analogous to that of the BCZYb electrolyte ($9.5 \times 10^{-6} \text{ K}^{-1}$) [20]. In contrast, the double perovskite NBSCF and BGLC show extraordinary high TECs. This indicates that the NBCFM is more beneficial in terms of long-term thermal stability and compatibility when it comes to cell fabrication.

3.3. Electrochemical evaluations of reversible protonic ceramic cells

The ASRs of the perovskite-structure materials were investigated in a symmetrical cell configuration using electrochemical impedance spectroscopy (EIS). Fig. 2d shows the ASRs, the key variable for distinguishing cathode activity [34], of the perovskite-based cells under open-circuit voltage (OCV) conditions. It should be noted that the NBCFM showed the lowest ASR (and also a lower activation energy of 0.97 eV) in the temperature range studied (i.e. $0.98 \Omega\cdot\text{cm}^2$ at 600°C), this result is much smaller than those of the highly active BSCF ($2.26 \Omega\cdot\text{cm}^2$) and BGLC ($1.82 \Omega\cdot\text{cm}^2$) at 600°C . In order to verify the excellent properties of the NBCFM electrode in RPCCs, perovskite cells were tested under PCFC and PCEC modes at $500\text{--}700^\circ\text{C}$ (Fig. 3a). The positive current density denotes PCFC operation, while the negative one refers to PCEC operation. The OCVs of the cells were at approximately 1.0 V, this indicates that the BCZYb electrolyte is fully dense. The PPDs of the NBCFM cell (with the pure NBCFM cathode) were very high, reaching $0.16\text{--}1.37 \text{ W}\cdot\text{cm}^{-2}$ at $500\text{--}700^\circ\text{C}$. In particular, the performance of the NBCFM cell in PCFC mode gives approximately 2–3 times the PPD of the PCFC with BGLC and BSCF cathode materials at 600°C (Fig. S4). The PPDs are compared with previously reported results at 600°C in Fig. 3b and Table 2 [12–14,35–43] and show an enormous improvement.

In PCEC mode, I–V curves of the cells using various steam electrode materials under a 20% steam/80% air atmosphere are also shown for comparison purposes. At each operating temperature, the current densities for PCEC with the NBCFM electrode at different applied voltages are much higher than those for the cells with other electrodes, this indicates that NBCFM is highly active during OER in PCEC. In particular, at 600°C , the performance in PCEC with the NBCFM steam electrode saw a dramatic increase to $-2.34 \text{ A}\cdot\text{cm}^{-2}$ at 1.4 V and 600°C (Fig. 3a), this is a remarkable value to achieve when we compare to the results of the cells with other steam electrodes: BSCF ($-0.37 \text{ A}\cdot\text{cm}^{-2}$), NBSCF ($-0.50 \text{ A}\cdot\text{cm}^{-2}$) and BGLC ($-0.37 \text{ A}\cdot\text{cm}^{-2}$) (Figs. 3b and S4). In addition, the pure NBCFM air electrode cell showed better performances than the composite NBCFM-NDC and NBCFM-BCZYb electrode cells under both PCFC and PCEC modes. More importantly, an extensive comparison of oxygen electrode activities of perovskite air (steam) electrodes reveals NBCFM to be one of the best-performing perovskite-based bifunctional

oxygen electrodes ever reported (Table 2) [12–14,35–43]. In addition, a further reduction in BCZYb thickness (from $\sim 20 \mu\text{m}$ in this work) is expected to boost cell performance by lowering its ohmic ASR ($0.127 \Omega\cdot\text{cm}^2$ at 600°C , Fig. S5) based on An et al. [17] who previously reported $1.3 \text{ W}\cdot\text{cm}^{-2}$ at 600°C with a very thin ($<5 \mu\text{m}$) $\text{BaCe}_{0.55}\text{Zr}_{0.3}\text{Y}_{0.15}\text{O}_{3-\delta}$ electrolyte (ASR of $0.09 \Omega\cdot\text{cm}^2$). Moreover, surface modification of the NBCFM triple perovskite air/steam electrode using infiltration techniques [16] and pulsed laser deposition [14] is an effective method to enhance the catalytic activity of RPCCs via extension of TPBs with increasing surface area.

The relevant Faraday efficiency (η) at each applied voltage and $500\text{--}600^\circ\text{C}$ was calculated using Faraday's law (Supplementary information) and was estimated at 99.4% under $-0.5 \text{ A}\cdot\text{cm}^{-2}$ at 500°C , suggesting that a BCZYb cell using the NBCFM steam electrode can generate the theoretically predicted amount of H_2 (Figs. 3d and S6). However, the Faradaic efficiency is decreased as the applied current and temperature increase because of the electronic leakage in the BCZYb electrolyte (p-type electronic conduction in oxidizing atmospheres) under PCEC mode. To confirm the reliability of the NBCFM electrode, a cycling test through PCFC and PCEC modes was designed where constant positive and negative current densities ($\pm 0.2 \text{ A}\cdot\text{cm}^{-2}$ for 24 h) were applied to the cell alternatively for 960 h, as seen in Fig. 3e. The cell voltage was maintained at approximately 0.9 V (in PCFC mode) and at 1.06 V (in PCEC mode) without any severe degradation in performance being seen over the entire process, this indicates that the NBCFM air (steam) electrode shows excellent bi-functional ORR and OER properties during PCFC and PCEC operation with outstanding stability.

3.4. Mechanistic study

The high concentrations of mobile oxygen defects in NBCFM (Fig. 1d) may contribute to better electrochemical performance as they lead to faster oxygen kinetics in OER and ORR. Fig. S5 shows an EIS plots of the perovskite air (steam) electrodes without an applied potential (at OCV) and with an applied potential of -0.20 (OER) and $0.20 \text{ A}\cdot\text{cm}^{-2}$ (ORR). The NBCFM cell shows the lowest R_{pol} in the temperature range studied under $0.2 \text{ A}\cdot\text{cm}^{-2}$ for ORR, $0.32 \Omega\cdot\text{cm}^2$ at 600°C , this result is lower than those for BSCF ($0.75 \Omega\cdot\text{cm}^2$), NBSCF ($0.73 \Omega\cdot\text{cm}^2$) and BGLC ($0.47 \Omega\cdot\text{cm}^2$) under the same conditions (Fig. 3f). Furthermore, the impedance arc of the NBCFM cell is significantly smaller than those of other perovskite-based cells under OER conditions of $-0.2 \text{ A}\cdot\text{cm}^{-2}$ ($0.35 \Omega\cdot\text{cm}^2$) at 600°C .

Further analysis was performed to investigate the electronic states of the perovskite-based electrodes. Fig. 4a shows the O 1s and Co 2p x-ray photoelectron spectroscopy (XPS) spectra (Fig. S7) of the perovskite materials. The four peaks at 532.9, 531.6, 530.6, and 528.2 eV can be assigned to the molecular water absorbed on the surface (H_2O), surface adsorbed oxygen (O_2/OH^-), highly oxidative oxygen species (O_2^-/O^-) and lattice oxygen species (O^{2-}), respectively [44]. The relative content (molar fraction) of these four oxygen species was estimated from the integrated area ratios of the sub-peaks. The increase in active atoms adjacent to oxygen vacancies facilitates OH^- adsorption kinetics and electron transport [44]. Based on the data (Fig. S7a), the relative content of the O_2^-/O^- species in the NBCFM surface (49.8%), which is correlated with the surface oxygen vacancies in catalysts, is higher than that of other perovskite materials. This means that there exists an abundance of surface oxygen vacancies in NBCFM, this is in agreement with the results of the nonstoichiometric oxygen measurements (TGA). Additionally, the transition metal ions (Co, Fe, Mn) doped into the B-site are beneficial to the adsorption/refilling of OH^- and desorption of O_2 under the enhanced charge transfer kinetics between the O 2p-band of the adsorbate and d-band of the B-site metal that are a result of this favorable modification to the electronic configuration of the triple perovskite structure [19–23].

As previously demonstrated, Co states are more relevant in

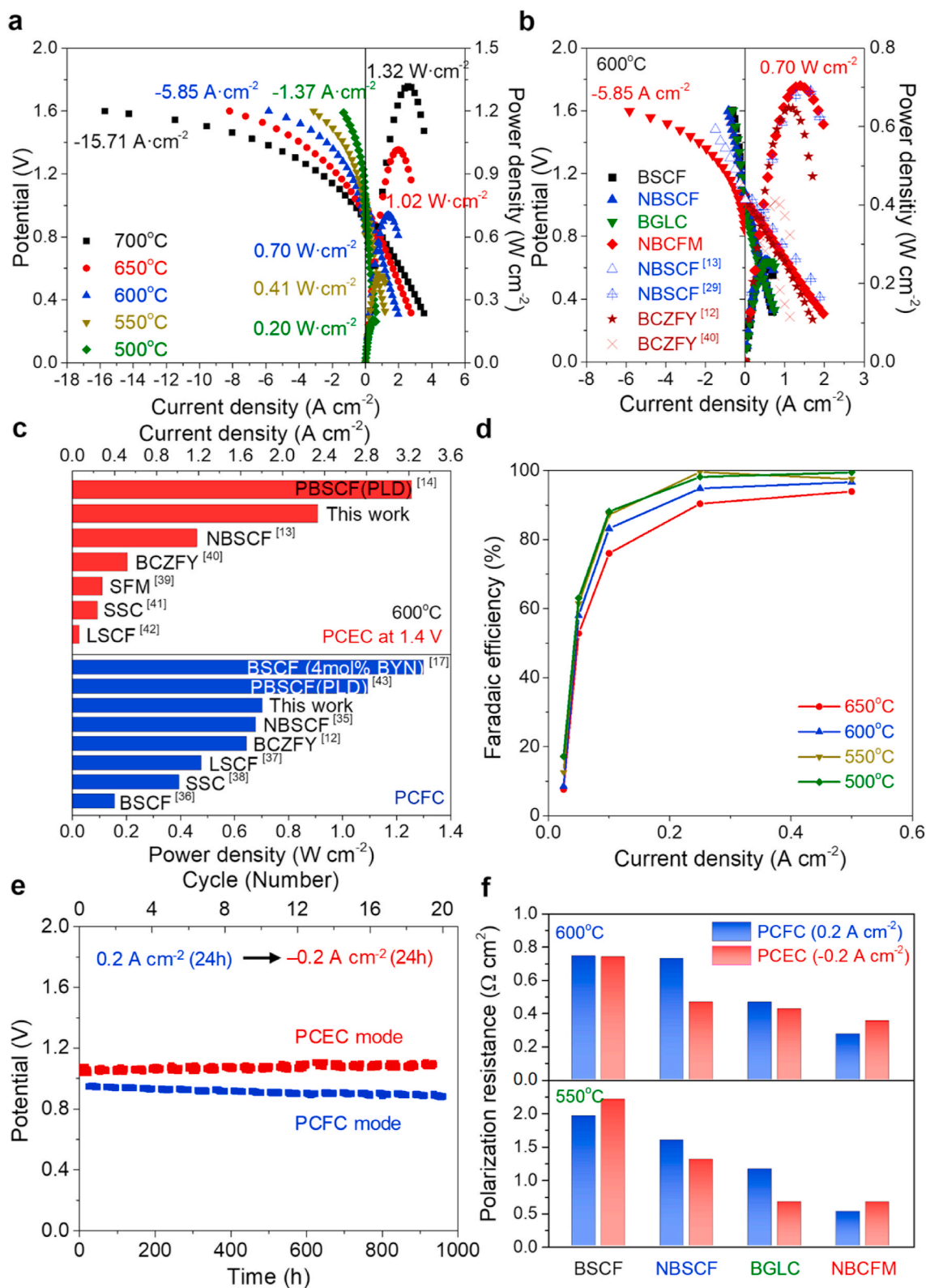


Fig. 3. Electrochemical performances and durability of the cells. (a) I–V characteristics of NBCFM cells in PCFC (under a supply of humidified H₂ and ambient air) and PCEC modes (under 20% steam/80% air in steam electrode and 10% H₂/90% N₂ in fuel electrode) at 500–700 °C. (b) I–V characteristics of perovskite-based cells in the PCFC and PCEC modes at 600 °C. (c) Performance comparison of PCFCs (maximum power density) and PCECs (current density at 1.4 V) with the previously reported bifunctional perovskite-based air (steam) electrode materials (BaY₂NiO₅; BYN). (d) Faradaic efficiency of NBCFM cell as a function of current density and temperatures. (e) Long-term durability of NBCFM cell for 960 h under the constant current density of 0.2 (for 24 h) and –0.2 A·cm⁻² (for 24 h) for PCFC and PCEC modes, respectively. (f) ASRs of perovskite air electrode cells under 0.2 A·cm⁻² for ORR and –0.2 A·cm⁻² for OER in RPCCs.

Table 2

Performance comparison of PCFCs and PCECs at 600 °C with the previously reported perovskite-based steam (air) electrode materials.

Ref.	Cell composition	Gas flow condition		Peak power density (W·cm ⁻²)	Current density at 1.4 V (A·cm ⁻²)
		Fuel electrode	Air electrode		
PCFC mode					
12	NiO-BCZYYb BCZYYb+1 wt% NiO BaCe _{0.6} Zr _{0.3} Y _{0.1} O ₃ -BCFZY			0.647	
17	NiO-BaCe _{0.55} Zr _{0.3} Y _{0.15} O ₃ BaCe _{0.55} Zr _{0.3} Y _{0.15} O ₃ +4 mol% BaY ₂ NiO ₅ BSCF			1.302	
35	NiO-BCZYYb BCZYYb NBSCF			0.680	
36	NiO-BaCe _{0.8} Y _{0.2} O ₃ BaCe _{0.8} Y _{0.2} O ₃ BSCF			0.282	
37	NiO-BCZYYb BCZYYb BaCe _{0.7} Zr _{0.1} Y _{0.2} O ₃ -LSCF			0.479	
38	NiO-BaCe _{0.7} Zr _{0.1} Y _{0.2} O ₃ BaCe _{0.5} Zr _{0.3} Y _{0.2} O _{3-δ} Sm _{0.5} Sr _{0.5} CoO ₃ .			0.396	
This work	NiO-BCZYYb BCZYYb NBCFM-NDC			0.704	
PCEC mode					
14	NiO-BaCe _{0.4} Zr _{0.4} Y _{0.1} Yb _{0.1} O ₃ BaCe _{0.4} Zr _{0.4} Y _{0.1} Yb _{0.1} O ₃ PBSCF (PLD) PBSCF	97% H ₂ /3% H ₂ O	97% Air/3% H ₂ O		3.235
13	NiO-BZCYYb BZCYYb NBSCF-BZCYYb	90% H ₂ /10% H ₂ O	90% Air/10% H ₂ O		1.190
39	Ni-BaZr _{0.8} Y _{0.2} O ₃ BaZr _{0.8} Y _{0.2} O ₃ Sr ₂ Fe _{1.5} Mo _{0.5} O ₆ -BaZr _{0.8} Y _{0.2} O ₃	10% H ₂ /90% N ₂	97% Air/3% H ₂ O		0.289
40	Ni-BaCe _{0.7} Zr _{0.1} Y _{0.1} Sm _{0.1} O ₃ BaCe _{0.7} Zr _{0.1} Y _{0.1} Sm _{0.1} O ₃ BaCe _{0.6} Zr _{0.3} Y _{0.1} O ₃ -BCZFY	97% H ₂ /3% H ₂ O	88% Air/12% H ₂ O		0.527
41	NiO-BaCe _{0.5} Zr _{0.3} Y _{0.2} O ₃ BaCe _{0.5} Zr _{0.3} Y _{0.2} O ₃ Sm _{0.5} Sr _{0.5} CoO ₃ -BaCe _{0.5} Zr _{0.3} Y _{0.2} O ₃	100% H ₂	50% Air/50% H ₂ O		0.241
42	NiO-BaZr _{0.9} Y _{0.1} O ₃ BaZr _{0.9} Y _{0.1} O ₃ BaZr _{0.8} Y _{0.2} O ₃ -La _{0.6} Sr _{0.1} Co _{0.2} Fe _{0.8} O ₃	4% H ₂ /96% Ar	97% Air/3% H ₂ O		0.069
This work	NiO-BCZYYb BCZYYb NBCFM	10% H ₂ /90% N ₂	80% Air/20% H ₂ O		2.341

influencing the electrochemical activities in oxygen electrode reactions [19,23]. The oxidation state of the Co was estimated via fitting the corresponding XPS spectra. The well deconvoluted profile in Fig. 4a of the Co 2p_{3/2} and Co 2p_{1/2} spectra at 779.5 and 794.6 eV, respectively, prove the coexistence of Co⁴⁺/Co³⁺. The ratio of Co⁴⁺/Co³⁺ in the perovskite structure can be calculated as per the respective area intensity of the characteristic peaks. The integrated area ratio of BSCF, BCZFY, NBSCF, BGLC, and NBCFM are 0.40, 0.40, 0.54, 0.54, and 0.56, respectively. These indicate that the generation of the high density of surface oxygen defects in NBCFM is caused by co-doping of multivalent ions.

We also performed first-principles calculations to confirm the outstanding catalytic effect of NBCFM compared to other perovskite-type catalysts, we found that our predictions based on first principles calculations are well matched with the experimentally confirmed results. It was reported that the small energy gap between the O 2p-band center and the Fermi level (E_F) results in outstanding oxygen activity from the perovskite-type catalysts [21]. Fig. 4b presents the energy gaps of the perovskites between E_F and the center of the O 2p projected density of state (pDOS). The energy at the highest DOS intensity was designated as the center of O 2p pDOS. BSCF delivers the smallest energy gap between E_F and the center of O 2p pDOS among the samples (Fig. S8). This kind of small energy gap (~1 eV) can result in structural instability, this, in turn, implies poor oxygen catalytic effect from BSCF. Grimaud et al. [21] demonstrated that moving the O p-band center closer to the E_F can increase oxygen electrode activity, but having the O p-band center too close to E_F decreases oxide stability and activity for oxygen electrode reactions. In the case of the other samples, it was predicted that the energy gap of NBCFM (~1.47 eV) is smaller than those of BCZFY (~2.05 eV) and NBSCF (~2.07 eV), which indicates that the catalytic effect of NBCFM is better than the other perovskite materials that are regarded as the outstanding ORR/OER catalysts in the group.

All the features described above are responsible for the faster reaction rate of the NBCFM during oxygen electrode reactions. The kinetic properties of the MIECs can be obtained from measurement of the transient response to a step change in the chemical potential by elec-

trical conductivity relaxation (ECR) [45]. Variations in the ambient atmosphere lead to changes in the charge carrier (oxygen vacancy) concentration of the MIEC, this manifests as a relaxation of the apparent macroscopic electrical conductivity. The ECR profiles of the perovskite materials were investigated during a sudden change in P_{O_2} ($-2.0 \leq \log(P_{O_2}/\text{atm}) \leq -0.68$) at 500–750 °C. Monotonic increases in the electrical conductivity were observed while reaching a new equilibrium value at a fixed P_{H_2O} (Fig. S9). The normalized electrical conductivity (Γ) relaxation profile describes a solution to Fick's second law [45–47]. D_{VO} represents the chemical diffusion coefficients [It should be noted that O²⁻ diffuses via vacancies ($v = V_O^{\bullet\bullet}$) in oxidizing (O) atmospheres]. Fig. 4c shows D_{VO} as a function of temperature during oxidation. It was found that D_{VO} increases with temperature during oxidation, and its values for the perovskite materials investigated in this work are on the same order of magnitude at similar temperatures when compared to data in previous literature (Table 3) [48,49]. Outstandingly, the D_{VO} value of NBCFM was much larger than that of the other perovskite cathode materials. A high D_{VO} value of $2.72 \times 10^{-4} \text{ cm}^2 \cdot \text{s}^{-1}$ at 600 °C was achieved for NBCFM (c.f. BSCF: 7.15×10^{-6} , NBSCF: 3.98×10^{-4} , BGLC: 1.10×10^{-4} , and BCZFY: $1.38 \times 10^{-4} \text{ cm}^2 \cdot \text{s}^{-1}$ at 600 °C) [49]. The activation energies for the D_{VO} of NBCFM obtained from the slope of the Arrhenius plot, as shown in Fig. 4c, was 0.76 eV.

Further investigations were undertaken through ECR measurements to scrutinize the impact of the hydration process ($-1.522 \leq \log(P_{H_2O}/\text{atm}) \leq -0.523$). As can be seen in Fig. S10, the ECR profiles of NBSCF and NBCFM show non-monotonic behaviors upon hydration (change of P_{H_2O}) at a fixed P_{O_2} (0.147 atm), while they show a monotonic increase with changes of P_{O_2} (oxidation) at a fixed P_{H_2O} . During hydration, when P_{H_2O} is abruptly increased from -1.522 to -0.523 for $\log(P_{H_2O}/\text{atm})$, the conductivity first decreased sharply to a minimum and then slowly increased to attain a new equilibrium value at 600–750 °C. Yoo et al. [50] reported that such non-monotonic twofold relaxation can be attributed to the decoupled chemical diffusion of H (or ambipolar diffusion of H⁺ and h^{*}) and O (or ambipolar diffusion of O²⁻ and 2h^{*}) components mediated by holes in the proton-conducting perovskite oxides, and not simple chemical diffusion of molecular water. The faster H-diffusion followed by slow O-diffusion leads to

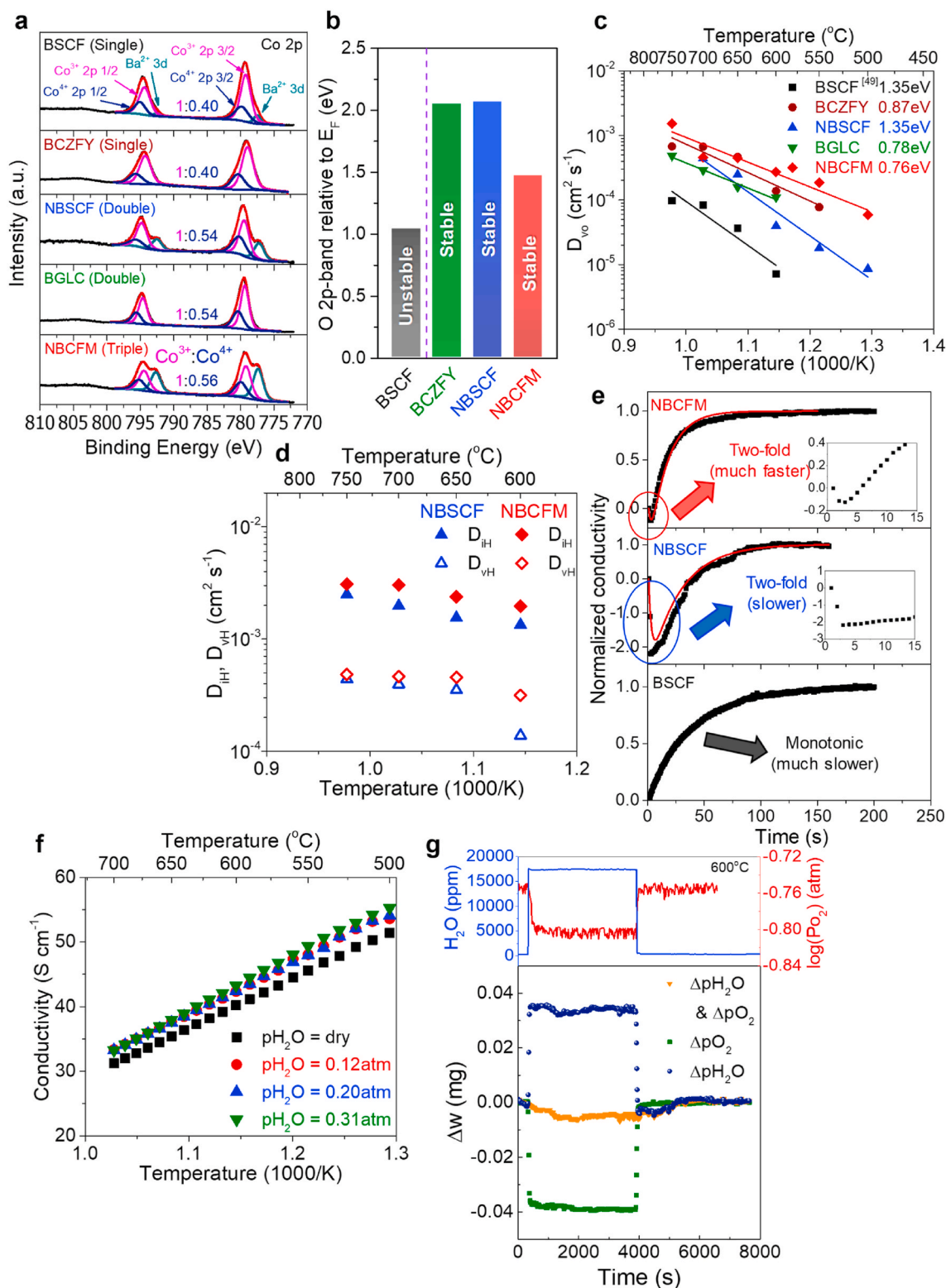


Fig. 4. Mechanistic analysis of NBCFM for oxygen electrode activity. (a) Co 2p XPS spectra of perovskite materials. (b) Energy gap between O 2p-band center and E_F on BSCF, BCZFY, NBSCF, and NBCFM. (c) Chemical diffusion coefficient (D_{vo}) of perovskite materials based on ECR measurement. (d) Decoupled chemical diffusivities of hydrogen (D_{iH}) and oxygen (D_{vH}) for NBCFM during hydration reaction at a fixed P_{O_2} . (e) ECR profiles for BSCF, NBSCF, and NBCFM during hydration process (P_{H_2O}) at a fixed P_{O_2} and 600 °C. (f) Conductivities of NBCFM (dense bar) under various P_{H_2O} at 500–600 °C using a DC 4-probe method. (g) Hydration property of the NBCFM under dry and wet air. Weight change (Δw) by changing P_{H_2O} at 600 °C.

Table 3Kinetic properties (D_{VO} , D_{IH} , and D_{VH}) of the perovskite materials, obtained from the ECR measurements.

Materials (Perovskite)	Temperature (°C)	Coefficients ($\text{cm}^2 \cdot \text{s}^{-1}$)		
		D_{VO}	D_{IH}	D_{VH}
BCZFY (Single)	550	7.72×10^{-5}		
	600	1.38×10^{-4}		
	650	4.64×10^{-4}		
	700	6.70×10^{-4}		
	750	6.77×10^{-4}		
BGLC (Double)	600	1.10×10^{-4}		
	650	1.58×10^{-4}		
	700	2.89×10^{-4}		
	750	4.86×10^{-4}		
NBSCF (Double)	500	8.61×10^{-6}		
	550	1.80×10^{-5}		
	600	3.98×10^{-5}	1.34×10^{-3}	1.38×10^{-4}
	650	2.48×10^{-4}	1.55×10^{-3}	3.52×10^{-4}
	700	4.41×10^{-4}	1.98×10^{-3}	3.95×10^{-4}
	750	N/A	2.49×10^{-3}	4.39×10^{-4}
NBCFM (Triple)	500	5.92×10^{-5}		
	550	1.86×10^{-4}		
	600	2.72×10^{-4}	1.96×10^{-3}	3.15×10^{-4}
	650	4.46×10^{-4}	2.38×10^{-3}	4.56×10^{-4}
	700	4.60×10^{-4}	3.03×10^{-3}	4.62×10^{-4}
	750	1.53×10^{-3}	3.08×10^{-3}	4.84×10^{-4}

non-monotonic ECR profiles with a transient change in the concentration of holes. The conductivity relaxation behavior of BSCF, however, showed a monotonic increase upon hydration, as verified by Lim et al. [51], that is different from that observed in NBSCF and NBCFM. These faster proton incorporation/release kinetics in NBCFM during hydration/dehydration could be the reason for the high ORR and OER performances in RPCCs.

To understand the transport properties of BSCF, NBSCF and NBCFM in wet atmospheres, the chemical diffusivities of hydrogen (D_{IH}) and oxygen (D_{VH}) during hydration (H) reactions were calculated by fitting the relaxation profiles [It should be noted that O^{2-} and H^+ diffuse via vacancies ($v = V_O^{\bullet\bullet}$) and interstitials ($i = H_i^+$ or OH_O^{\bullet}), respectively] [50, 51]. The values of D_{IH} are always higher than that of D_{VH} over the entire range of temperatures and P_{H_2O} levels studied, this indicates that the chemical diffusion of protons is always higher than that of oxygen-ions during hydration (Table 3). More importantly, the D_{IH} and D_{VH} of NBCFM were much higher than those of BSCF and NBSCF with changes in P_{H_2O} atmosphere, as shown in Fig. 4d and e. That is, the oxygen defect-rich structure of triple perovskite NBCFM resulted enhanced reaction kinetics of oxygen electrodes in RPCCs via incorporation of water vapor into the perovskite structure.

Further evidence supporting the triple-conducting properties of

NBCFM is based on their conductivities measured under various humidity conditions. As shown in Fig. 4f, the conductivities of NBCFM increase with an increase in P_{H_2O} from dry to wet (12–31%) air at 500–700 °C. The conductivity of NBCFM under dry air is $40.2 \text{ S} \cdot \text{cm}^{-1}$, which is increased to $43.3 \text{ S} \cdot \text{cm}^{-1}$ at 600 °C when 31% H_2O mixed air was supplied, suggesting the excellent proton conduction of NBCFM. The weight change (Δw) was also measured by applying thermogravimetric analysis to confirm the hydration characteristics of the triple perovskite exhibiting multi-ion conduction property (Figs. 4g and S11). When changing from dry air ($P_{O_2}/\text{atm} = 1.70 \times 10^{-1}$) to wet air ($P_{O_2}/\text{atm} = 1.58 \times 10^{-1}$) at 700 °C, the change in oxygen partial pressure is not small enough for ignoring any weight change from reduction reaction for highly defective oxides, like triple perovskite. Therefore, the pure water vapor partial pressure effect by hydration on weight change may be calculated by removing oxygen partial pressure driven weight change from the result of changing both the oxygen and water vapor partial pressure, simultaneously (Table S1 and Fig. S12). As shown in Fig. 4g (Figs. S11 and S12), when the oxygen partial pressure decreases at a dry condition, a mass change of about 45 μg is observed (as shown in green), but when both oxygen and water vapor pressure change at the same time, a mass decrease is about 10 μg (as shown in orange). Therefore, the effect of pure water vapor partial pressure on weight change can be calculated as shown in blue from the difference between the two results, around +35 μg . Even considering that the initial specimen weighed around 0.997 g, it could be confirmed that a considerable amount of water vapor was incorporated into the specimen.

4. Conclusions

We have demonstrated that our triple perovskite NBCFM exhibits the highest reported activity for ORR and OER in IT-RPCCs. The high power density of the PCFCs was achieved using our NBCFM cathode on account of its superior ORR activity compared to other perovskite materials. In addition, a current density of $-2.34 \text{ A} \cdot \text{cm}^{-2}$ was achieved under a 1.4 V electrolyzing potential at 600 °C. Furthermore, the cell voltage was maintained at 0.9 V ($0.2 \text{ A} \cdot \text{cm}^{-2}$) and 1.06 V ($-0.2 \text{ A} \cdot \text{cm}^{-2}$) without any severe degradation in performance over the course of the durability test. The superior electrocatalytic performance of NBCFM in oxygen electrode reactions is attributed to its high concentration of surface oxygen defects, favorable electronic configuration and coordination chemistry in the triple perovskite structure, hydration property, and rapid reaction rates for steam and air electrodes.

CRediT authorship contribution statement

John-In Lee: Conceptualization, Methodology, Investigation, Validation, Formal analysis, Visualization, Writing – review & editing. **Hyunyoung Park:** Software, Formal analysis, Data curation, Visualization. **Hohan Bae:** Methodology, Investigation, Validation, Formal analysis. **Muhammad Saqib:** Methodology, Investigation, Validation, Formal analysis. **Kwangho Park:** Conceptualization, Methodology, Investigation, Formal analysis, Writing – original draft, Methodology, Investigation, Validation, Formal analysis. **Ji-Seop Shin:** Methodology, Investigation, Validation, Formal analysis. **Minkyong Jo:** Methodology, Investigation, Validation, Formal analysis. **Jongsoon Kim:** Software, Formal analysis, Data curation, Resources, Visualization, Writing – review & editing. **Sun-Ju Song:** Conceptualization, Methodology, Resources, Supervision, Writing – review & editing. **Eric D. Wachsman:** Methodology, Supervision, Writing – review & editing. **Jun-Young Park:** Conceptualization, Methodology, Funding acquisition, Supervision, Writing – review & editing.

Declaration of competing interest

The authors declare that they have no known competing financial interests or personal relationships that could have appeared to influence

the work reported in this paper.

Acknowledgements

This research was supported by the Core Technology Development Program to Future Hydrogen Energy and Basic Science Research Program through the National Research Foundation of Korea (NRF-2021M313A1084830 & NRF-2019H1D8A2106002) and by the Industrial Technology Innovation R&D Program of the Korea Institute of Energy Technology Evaluation and Planning (KETEP), which has been granted financial resources from the Ministry of Trade, Industry & Energy, Republic of Korea (No. 20203010030020).

Appendix A. Supplementary data

Supplementary data to this article can be found online at <https://doi.org/10.1016/j.jpowsour.2021.230409>.

References

- [1] M.C. Williams, J.P. Strakey, W.A. Surdoyal, L.C. Wilson, Solid oxide fuel cell technology development in the U.S., *Solid State Ionics* 177 (2006) 2039–2044, <https://doi.org/10.1016/j.ssi.2006.02.051>.
- [2] E.D. Wachsman, C.M. Marlowe, K.T. Lee, Role of solid oxide fuel cells in a balanced energy strategy, *Energy Environ. Sci.* 5 (2012) 5498–5509, <https://doi.org/10.1039/C1EE02445K>.
- [3] S.H. Jensen, H. Langnickel, N. Hintzen, M. Chen, X. Sun, A. Hauch, G. Butera, L. R. Clausen, Reversible operation of a pressurized solid oxide cell stack using carbonaceous gases, *J. Energy Storag.* 22 (2019) 106–115, <https://doi.org/10.1016/j.est.2019.02.003>.
- [4] M. Götz, J. Lefebvre, F. Mörs, A.M. Koch, F. Graf, S. Bajohr, R. Reimert, T. Kolb, Renewable Power-to-Gas: a technological and economic review, *Renew. Energy* 85 (2016) 1371–1390, <https://doi.org/10.1016/j.renene.2015.07.066>.
- [5] M.A. Laguna-Bercero, J.A. Kilner, S.J. Skinner, Development of oxygen electrodes for reversible solid oxide fuel cells with scandia stabilized zirconia electrolytes, *Solid State Ionics* 192 (2011) 501–504, <https://doi.org/10.1016/j.ssi.2010.01.003>.
- [6] M.-B. Choi, B. Singh, E.D. Wachsman, S.-J. Song, Performance of $\text{La}_{0.1}\text{Sr}_{0.9}\text{Co}_{0.8}\text{Fe}_{0.2}\text{O}_{3-\delta}$ and $\text{La}_{0.1}\text{Sr}_{0.9}\text{Co}_{0.8}\text{Fe}_{0.2}\text{O}_{3-\delta}-\text{Ce}_{0.9}\text{Gd}_{0.1}\text{O}_2$ oxygen electrodes with $\text{Ce}_{0.9}\text{Gd}_{0.1}\text{O}_2$ barrier layer in reversible solid oxide fuel cells, *J. Power Sources* 239 (2013) 361–373, <https://doi.org/10.1016/j.jpowsour.2013.03.154>.
- [7] S.Y. Gómez, D. Hotza, Current developments in reversible solid oxide fuel cells, *Renew. Sustain. Energy Rev.* 61 (2016) 155–174, <https://doi.org/10.1016/j.rser.2016.03.005>.
- [8] M.A. Laguna-Bercero, S.J. Skinner, J.A. Kilner, Performance of solid oxide electrolysis cells based on scandia stabilised zirconia, *J. Power Sources* 192 (2009) 126–131, <https://doi.org/10.1016/j.jpowsour.2008.12.139>.
- [9] E. Fabbri, L. Bi, D. Pergolesi, E. Traversa, Towards the next generation of solid oxide fuel cells operating below 600 °C with chemically stable proton-conducting electrolytes, *Adv. Mater.* 24 (2012) 195–208, <https://doi.org/10.1002/adma.201103102>.
- [10] L. Yang, S. Wang, K. Blinn, M. Liu, Z. Liu, Z. Cheng, M. Liu, Enhanced sulfur and coking tolerance of a mixed ion conductor for SOFCs: $\text{BaZr}_{0.1}\text{Ce}_{0.7}\text{Y}_{0.2-x}\text{Yb}_x\text{O}_{3-\delta}$, *Science* 326 (2009) 126–129, <https://doi.org/10.1126/science.1174811>.
- [11] C. Duan, R.J. Kee, H. Zhu, C. Karakaya, Y. Chen, S. Ricote, A. Jarry, E.J. Crumlin, D. Hook, R. Braun, N.P. Sullivan, R. O'Hayre, Highly durable, coking and sulfur tolerant, fuel-flexible protonic ceramic fuel cells, *Nature* 557 (2018) 217–222, <https://doi.org/10.1038/s41586-018-0082-6>.
- [12] C. Duan, J. Tong, M. Shang, S. Nikodemski, M. Sanders, S. Ricote, A. Almansoori, R. O'Hayre, Readily processed protonic ceramic fuel cells with high performance at low temperatures, *Science* 346 (2015) 1321–1326, <https://doi.org/10.1126/science.aab3987>.
- [13] J. Kim, A. Jun, O. Gwon, S. Yoo, M. Liu, J. Shin, T.-H. Lim, G. Kim, Hybrid-solid oxide electrolysis cell: a new strategy for efficient hydrogen production, *Nano Energy* 44 (2018) 121–126, <https://doi.org/10.1016/j.nanoen.2017.11.074>.
- [14] S. Choi, T.C. Davenport, S.M. Haile, Protonic ceramic electrochemical cells for hydrogen production and electricity generation: exceptional reversibility, stability, and demonstrated faradaic efficiency, *Energy Environ. Sci.* 12 (2019) 206–215, <https://doi.org/10.1039/C8EE02865F>.
- [15] R. Zohourian, R. Merkle, G. Raimondi, J. Maier, Mixed-conducting perovskites as cathode materials for protonic ceramic fuel cells: understanding the trends in proton uptake, *Adv. Funct. Mater.* 28 (2018) 801241, <https://doi.org/10.1002/adfm.201801241>.
- [16] M. Saqib, J.-I. Lee, J.-S. Shin, K. Park, Y.-D. Kim, K.B. Kim, J.H. Kim, H.-T. Lim, J.-Y. Park, Modification of oxygen-ionic transport barrier of $\text{BaCo}_{0.4}\text{Zr}_{0.1}\text{Fe}_{0.4}\text{Y}_{0.1}\text{O}_3$ steam (air) electrode by impregnating samarium-doped ceria nanoparticles for proton-conducting reversible solid oxide cells, *J. Electrochem. Soc.* 12 (2019), <https://doi.org/10.1149/2.0461912jes>, F746–F754.
- [17] H. An, H.-W. Lee, B.-K. Kim, J.-W. Son, K.J. Yoon, H. Kim, D. Shin, H.-I. Ji, J.-H. Lee, A $5 \times 5 \text{ cm}^2$ protonic ceramic fuel cell with a power density of 1.3 W cm^{-2} at 600 °C, *Nat. Energy* 3 (2018) 870–875, <https://doi.org/10.1038/s41560-018-0230-0>.
- [18] R. Strandbakke, V.A. Cherepanov, A.Y. Zuev, D.S. Tsvetkov, C. Argiris, G. Sourkouni, S. Prünke, T. Norby, Gd- and Pr-based double perovskite cobaltites as oxygen electrodes for proton ceramic fuel cells and electrolyser cells, *Solid State Ionics* 278 (2015) 120–132, <https://doi.org/10.1016/j.ssi.2015.05.014>.
- [19] N.-I. Kim, Y.J. Sa, T.S. Yoo, S.R. Choi, R.A. Afzal, T. Choi, Y. Seo, K. Lee, J. Y. Hwang, W.S. Choi, S.H. Joo, J.-Y. Park, Oxygen-deficient triple perovskites as highly active and durable bifunctional electrocatalysts for oxygen electrode reactions, *Sci. Adv.* 4 (2018), <https://doi.org/10.1126/sciadv.aap9360> eaap9360.
- [20] L. Zhang, S. Yang, S. Zhang, Y. Yang, Cerium and gadolinium co-doped perovskite oxide for a protonic ceramic fuel cell cathode, *Int. J. Hydrogen Energy* 44 (2019) 27921–27929, <https://doi.org/10.1016/j.ijhydene.2019.09.057>.
- [21] A. Grimaud, K.J. May, C.E. Carlton, Y.-L. Lee, M. Risch, W.T. Hong, J. Zhou, S.-H. Yang, *Nat. Commun.* 4 (2013) 2439, <https://doi.org/10.1038/ncomms3439>.
- [22] J.-I. Jung, M. Risch, S. Park, M.G. Kim, G. Nam, H.-Y. Jeong, S.-H. Yang, J. Cho, *Energy Environ. Sci.* 9 (2016) 176–183, <https://doi.org/10.1039/C5EE03124A>.
- [23] W.T. Hong, K.A. Stoerzinger, Y.-L. Lee, L. Giordano, A. Grimaud, A.M. Johnson, J. Hwang, E.J. Crumlin, W. Yange, S.-H. Yang, *Energy Environ. Sci.* 10 (2017) 2190–2200, <https://doi.org/10.1039/C7EE02052J>.
- [24] G. Kresse, D. Joubert, From ultrasoft pseudopotentials to the projector augmented-wave method, *Phys. Rev. B Condens. Matter* 59 (1999) 1758–1775, <https://doi.org/10.1103/PhysRevB.59.1758>.
- [25] P.E. Blöchl, Projector augmented-wave method, *Phys. Rev. B Condens. Matter* 50 (1994) 17953–17979, <https://doi.org/10.1103/PhysRevB.50.17953>.
- [26] B. Hammer, L.B. Hansen, J.K. Nørskov, Improved adsorption energetics within density-functional theory using revised Perdew-Burke-Ernzerhof functionals, *Phys. Rev. B Condens. Matter* 59 (1999) 7413–7421, <https://doi.org/10.1103/PhysRevB.59.7413>.
- [27] J.P. Perdew, K. Burke, M. Ernzerhof, Generalized gradient approximation made simple, *Phys. Rev. Lett.* 77 (1996) 3865–3868, <https://doi.org/10.1103/PhysRevLett.77.3865>.
- [28] Y.-F. Li, A. Selloni, Mechanism and activity of water oxidation on selected surfaces of pure and Fe-doped NiO_x , *ACS Catal.* 4 (2014) 1148–1153, <https://doi.org/10.1021/cs401245q>.
- [29] A. Van der Ven, J.C. Thomas, Q. Xu, J. Bhattacharya, Linking the electronic structure of solids to their thermodynamic and kinetic properties, *Math. Comput. Simulat.* 80 (2010) 1393–1410, <https://doi.org/10.1016/j.matcom.2009.08.008>.
- [30] Z. Yang, A.S. Harvey, A. Infortuna, F. Schoonman, L.J. Gauckler, Electrical conductivity and defect chemistry of $\text{Ba}_x\text{Sr}_{1-x}\text{Co}_y\text{Fe}_{1-y}\text{O}_{3-\delta}$ perovskites, *J. Solid State Electrochem.* 15 (2011) 277–284, <https://doi.org/10.1007/s10008-010-1208-4>.
- [31] A.V. Kovalevsky, A.A. Yaremchenko, V.A. Kolotygin, A.L. Shaula, V.V. Kharton, F. M.M. Snijkers, A. Buekenhoudt, J.R. Frade, E.N. Naumovich, Processing and oxygen permeation studies of asymmetric multilayer $\text{Ba}_{0.5}\text{Sr}_{0.5}\text{Co}_{0.8}\text{Fe}_{0.2}\text{O}_{3-\delta}$ membranes, *J. Membr. Sci.* 380 (2011) 68–80, <https://doi.org/10.1016/j.memsci.2011.06.034>.
- [32] P. Batocchi, F. Mauvy, S. Fourcade, M. Parco, Electrical and electrochemical properties of architected electrodes based on perovskite and A_2MO_4 -type oxides for protonic ceramic fuel cell, *Electrochim. Acta* 145 (2014) 1–10, <https://doi.org/10.1016/j.electacta.2014.07.001>.
- [33] G. Ch. Kostoglou, P. Fertis, Ch. Ftikos, The perovskite oxide system $\text{Pr}_{1-x}\text{Sr}_x\text{Co}_{1-y}\text{Mn}_y\text{O}_{3-\delta}$: crystal structure and thermal expansion, *J. Eur. Ceram. Soc.* 18 (1998) 2209–2215, [https://doi.org/10.1016/S0955-2219\(98\)00169-1](https://doi.org/10.1016/S0955-2219(98)00169-1).
- [34] M. Shang, J. Tong, R. O'Hayre, A promising cathode for intermediate temperature protonic ceramic fuel cells: $\text{BaCo}_{0.4}\text{Fe}_{0.4}\text{Zr}_{0.2}\text{O}_{3-\delta}$, *RSC Adv.* 3 (2013) 15769–15775, <https://doi.org/10.1039/C3RA41828F>.
- [35] J. Kim, S. Sengodan, G. Kwon, D. Ding, J. Shin, M. Liu, G. Kim, Triple-conducting layered perovskites as cathode materials for proton-conducting solid oxide fuel cells, *ChemSusChem* 7 (2014) 2811–2815, <https://doi.org/10.1002/cssc.201402351>.
- [36] Y. Guo, Y. Lin, R. Ran, Z. Shao, Zirconium doping effect on the performance of proton-conducting $\text{BaZr}_y\text{Ce}_{0.8-y}\text{Y}_{0.2}\text{O}_{3-\delta}$ ($0.0 \leq y \leq 0.8$) for fuel cell applications, *J. Power Sources* 193 (2009) 400–407, <https://doi.org/10.1016/j.jpowsour.2009.03.044>.
- [37] N.T.Q. Nguyen, H.H. Yoon, Preparation and evaluation of $\text{BaZr}_{0.1}\text{Ce}_{0.7}\text{Y}_{0.1}\text{Yb}_{0.1}\text{O}_{3-\delta}$ (BZCYYb) electrolyte and BZCYYb-based solid oxide fuel cells, *J. Power Sources* 231 (2013) 213–218, <https://doi.org/10.1016/j.jpowsour.2013.01.011>.
- [38] Z. Shi, W. Sun, W. Liu, Synthesis and characterization of $\text{BaZr}_{0.3}\text{Ce}_{0.5}\text{Y}_{0.2-x}\text{Yb}_x\text{O}_{3-\delta}$ proton conductor for solid oxide fuel cells, *J. Power Sources* 245 (2014) 953–957, <https://doi.org/10.1016/j.jpowsour.2013.07.060>.
- [39] L. Lei, Z. Tao, X. Wang, J.P. Lemmond, F. Chen, Intermediate-temperature solid oxide electrolysis cells with thin proton-conducting electrolyte and a robust air electrode, *J. Mater. Chem. A* 5 (2017) 22945–22951, <https://doi.org/10.1039/C7TA05841A>.
- [40] Y. Meng, J. Gao, H. Huang, M. Zou, J. Duffy, J. Tong, K.S. Brinkman, A high-performance reversible protonic ceramic electrochemical cell based on a novel Sm-doped $\text{BaCe}_{0.7}\text{Zr}_{0.1}\text{Y}_{0.2}\text{O}_{3-\delta}$ electrolyte, *J. Power Sources* 439 (2019) 227093, <https://doi.org/10.1016/j.jpowsour.2019.227093>.
- [41] F. He, D. Song, R. Peng, G. Meng, S. Yang, Electrode performance and analysis of reversible solid oxide fuel cells with proton conducting electrolyte of $\text{BaCe}_{0.5}\text{Zr}_{0.3}\text{Y}_{0.2}\text{O}_{3-\delta}$, *J. Power Sources* 195 (2010) 3359–3364, <https://doi.org/10.1016/j.jpowsour.2009.12.079>.

- [42] L. Bi, S.P. Shafi, E. Traversa, Y-doped BaZrO₃ as a chemically stable electrolyte for proton-conducting solid oxide electrolysis cells (SOECs), *J. Mater. Chem. A* 3 (2015) 5815–5819, <https://doi.org/10.1039/C4TA07202B>.
- [43] S. Choi, C.J. Kucharczyk, Y. Liang, X. Zhang, I. Takeuchi, H.-I. Ji, S.M. Haile, Exceptional power density and stability at intermediate temperatures in protonic ceramic fuel cells, *Nat. Energy* 3 (2018) 202–210, <https://doi.org/10.1038/s41560-017-0085-9>.
- [44] X. Li, J. Zhang, Q. Feng, C. Pu, L. Zhang, M. Hu, X. Zhou, X. Zhong, W. Yi, J. Tang, Z. Li, X. Zhao, H. Li, B. Xu, Redox inactive ion meliorated BaCo_{0.4}Fe_{0.4}Zr_{0.1}Y_{0.1}O_{3-δ} perovskite oxides as efficient electrocatalysts for the oxygen evolution reaction, *J. Mater. Chem. A* 6 (2018) 17288–17296, <https://doi.org/10.1039/C8TA05599H>.
- [45] H.-I. Yoo, C.-E. Lee, Conductivity relaxation patterns of mixed conductor oxides under a chemical potential gradient, *Solid State Ionics* 180 (2009) 326–337, <https://doi.org/10.1016/j.ssi.2009.01.001>.
- [46] J.A. Lane, J.A. Kilner, Measuring oxygen diffusion and oxygen surface exchange by conductivity relaxation, *Solid State Ionics* 136–137 (2000) 997–1001, [https://doi.org/10.1016/S0167-2738\(00\)00554-3](https://doi.org/10.1016/S0167-2738(00)00554-3).
- [47] S. Wang, P.A.W. van der Heide, C. Chavez, A.J. Jacobson, S.B. Adler, An electrical conductivity relaxation study of La_{0.6}Sr_{0.4}Fe_{0.8}Co_{0.2}O_{3-δ}, *Solid State Ionics* 156 (2003) 201–208, [https://doi.org/10.1016/S0167-2738\(02\)00178-9](https://doi.org/10.1016/S0167-2738(02)00178-9).
- [48] M. Li, Y. Wang, Y. Wang, F. Chen, C. Xia, Bismuth doped lanthanum ferrite perovskites as novel cathodes for intermediate-temperature solid oxide fuel cells, *ACS Appl. Mater. Interfaces* 6 (2014) 11286–11294, <https://doi.org/10.1021/am5017045>.
- [49] P.F. Haworth, S. Smart, J.M. Serra, J.C. Diniz da Costa, Combined investigation of bulk diffusion and surface exchange parameters of silver catalyst coated yttrium-doped BSCF membranes, *Phys. Chem. Chem. Phys.* 14 (2012) 9104–9111, <https://doi.org/10.1039/C2CP41226H>.
- [50] E. Kim, H.-I. Yoo, Two-fold-to-single-fold transition of the conductivity relaxation patterns of proton-conducting oxides upon hydration/dehydration, *Solid State Ionics* 252 (2013) 132–139, <https://doi.org/10.1016/j.ssi.2013.04.005>.
- [51] D.-K. Lim, B. Singh, M.-B. Cho, S.-J. Song, Study of hydration/dehydration kinetics of SOFC cathode material Ba_{0.5}Sr_{0.5}Co_{0.8}Fe_{0.2}O_{3-δ} by electrical conductivity relaxation technique, *J. Electrochem. Soc.* 160 (2013), <https://doi.org/10.1149/2.021308jes>. F764–F768.